Research Square

Preprints are preliminary reports that have not undergone peer review.
They should not be considered conclusive, used to inform clinical practice,
or referenced by the media as validated information.

Handheld digital biopsy device for intraoperative assessment of surgical margins during partial nephrectomy

Seungmin Lee
Korea Institute of Industrial Technology
Yangkyu Park
Chonnam National University
Sung Sun Kim
Chonnam National University Hospital
Sangyul Baik
Sungkyunkwan University
Ho Seok Chung
Chonnam National University Hospital
Jinhwan Kim
jinhwan@kitech.re.kr

Korea Institute of Industrial Technology

Article

Keywords: Digital biopsy, Biosensor, Impedance, Surgical margin, Partial nephrectomy, Carcinoma

Posted Date: November 16th, 2026

DOI: https://doi.org/10.21203/rs.3.rs-11505351/v1

License: This work is licensed under a Creative Commons Attribution 4.0 International License.
Read Full License

Additional Declarations: No competing interests reported.

Handheld digital biopsy device for intraoperative assessment of surgical margins during partial nephrectomy

Seungmin Lee [1,4], Yangkyu Park [2], Sung Sun Kim [3], Sangyul Baik[4], Ho Seok Chung [5 *], Jinhwan Kim [1 *]

[1] Industrial Transformation Technology Department, Research Institute of Sustainable Development Technology, Korea Institute of Industrial Technology, Cheonan-Si, Chungcheongnam-do 31056, Republic of Korea

[2] Department of Mechatronics Engineering, Chonnam National University, 50 Daehak-ro, Yeosu, 59626, Jeonnam, Republic of Korea

[3] Department of Pathology, Chonnam National University Hospital, Chonnam National University Medical School, 61469, Gwangju, Republic of Korea.

[4] Department of Mechanical Engineering, Sungkyunkwan University, 16419, Suwon, Republic of Korea.

[5] Department of Urology, Chonnam National University Hospital, Chonnam National University Medical School, 61469, Gwangju, Republic of Korea.

[*] **Co-corresponding authors**: Jinhwan Kim (E-mail address: jinhwan@kitech.re.kr) and Ho Seok Chung (E-mail address: hschung615@gmail.com)

Abstract

Partial nephrectomy requires reliable discrimination between renal carcinoma and adjacent renal parenchyma to achieve negative surgical margins while preserving functional tissue. In this study, we developed a handheld digital biopsy (HDB) device integrating impedance and force sensors for intraoperative surgical margin assessment. The impedance sensor incorporating bipolar electrodes was fabricated using a microelectromechanical systems (MEMS) process. Its discrimination capability was evaluated using solutions with different conductivities. To generalize the sensor output, a calibration curve (R^2 = 0.99) was established to estimate conductivity from impedance measurements at the optimal frequency, at which the largest impedance difference was observed. Subsequently, electrical impedance was measured in ex-vivo human papillary renal cell carcinoma (pRCC), clear cell renal cell carcinoma (ccRCC), and their corresponding adjacent renal parenchyma (pAP and cAP) under a constant contact force. The impedance of both carcinomas was significantly lower than that of their corresponding parenchyma across the measured frequency range ($p < 0.05$). The estimated conductivities of pRCC, pAP, ccRCC, and cAP were 0.16 ± 0.03, 0.01 ± 0.002, 1.03 ± 0.05, and 0.79 ± 0.09 S/m, respectively ($p < 0.0001$). These results demonstrate the feasibility of the HDB device for intraoperative renal carcinoma discrimination.

Keywords: Digital biopsy, Biosensor, Impedance, Surgical margin, Partial nephrectomy, Carcinoma

Introduction

Renal cell carcinoma (RCC) accounts for approximately 2–3% of all adult malignancies, with an estimated 434,000 new cases worldwide in 2022 [1]. RCC comprises several histological subtypes, among which clear cell RCC (ccRCC) and papillary RCC (pRCC) account for approximately 70–80% and 10–15% of cases, respectively [2,3]. With the widespread use of abdominal imaging, an increasing proportion of RCC cases is now detected incidentally as small, asymptomatic, organ-confined masses rather than through the classic triad of flank pain, gross hematuria, and a palpable mass [2]. This stage migration has established partial nephrectomy (PN), rather than radical nephrectomy, as the recommended reference standard for clinical T1 renal masses because it preserves functioning nephrons without compromising oncological control [3]. This benefit is particularly relevant for elderly or comorbid patients with pre-existing chronic kidney disease, in whom further nephron loss can accelerate renal and cardiovascular morbidity [3,5].

PN, however, requires precise delineation of the tumor–parenchyma interface, which is often demarcated only by a fibrous pseudocapsule of variable thickness and integrity. A resection plane placed too close to the tumor can result in a positive surgical margin, which is independently associated with a two-fold increase in recurrence risk, rising to more than seven-fold in tumors with adverse pathological features, such as pT2–3a stage or high nuclear grade [4]. A positive surgical margin also necessitates intensified surveillance and, in selected cases, re-resection or completion nephrectomy [3]. Conversely, a resection plane placed too far from the tumor unnecessarily sacrifices functional parenchyma. Indeed, the volume of preserved renal parenchyma, rather than the duration of warm ischemia, is the dominant modifiable determinant of long-term renal function after surgery [5].

In current practice, this boundary is delineated using intraoperative ultrasonography (IOUS). Using a drop-in or laparoscopic transducer, the surgeon delineates the tumor contour, depth, and relationship to the collecting system on B-mode imaging and then marks the intended resection line on the renal capsule using monopolar electrocautery [6]. The resulting margin is therefore largely based on subjective, operator-dependent judgment. Surgeons may compensate for uncertainty by adding a generous safety margin at the expense of healthy parenchyma, whereas less experienced surgeons may be more prone to breaching the pseudocapsule. The tumor–parenchyma interface is frequently indistinct, particularly in isoechoic, completely endophytic, or cystic lesions, and the two-dimensional sonographic contour must be mentally transposed onto the three-dimensional renal surface. Acoustic shadowing and oblique insonation angles can further distort the apparent boundary. Moreover, robot-assisted surgery eliminates much of the haptic feedback that facilitates tumor localization during open surgery. Intraoperative frozen-section analysis does not fully resolve these limitations because it prolongs operative time, samples only a small portion of the resection surface, is susceptible to electrocautery artifacts, and rarely alters clinical management [7]. Consequently, no objective, quantitative, and immediate readout of tissue identity is currently available at the intended

resection line.

To overcome these limitations, we propose a handheld digital biopsy (HDB) device that can discriminate renal carcinoma from renal parenchyma based on differences in tissue electrical impedance during surgery. Electrical impedance is an important analytical indicator in biosensing and has been applied to various biological analyses, including single-cell analysis [8–10], tissue characterization [11–13], and virus detection [14–16]. The developed HDB device integrates an impedance sensor to measure the electrical properties of tissue and a force sensor to monitor the contact force applied to the tissue in real time. To enable tissue discrimination within a localized area, an impedance sensor with bipolar electrodes was fabricated on a polyimide film using a microelectromechanical systems (MEMS) process. The discrimination capability of the impedance sensor was first evaluated in a preliminary experiment using solutions with different conductivities. Subsequently, the electrical impedance of renal tissues resected from clinical patients was measured over a frequency range of 0.7 kHz to 2 MHz. Because variations in contact force can deform the tissue at the electrode–tissue interface and thereby affect the measured sensor output, the electrical impedance of each tissue sample was measured under a constant contact-force condition. In this study, papillary renal cell carcinoma (pRCC) and clear cell renal cell carcinoma (ccRCC), which are major subtypes of RCC, and their corresponding renal parenchyma were evaluated under the guidance of a clinician. Given the intended real-time intraoperative application of the HDB device, we also developed a method for estimating tissue conductivity from the measured impedance. Finally, the differences in conductivity between pRCC and ccRCC and their corresponding renal parenchyma were analyzed in relation to their histological characteristics and associated biological mechanisms.

Methods

Device design and fabrication

As shown in Fig. 1(a), determining an optimal surgical margin is important for ensuring oncological safety while preserving renal function after partial nephrectomy. Accordingly, an HDB device was developed for the intraoperative evaluation of surgical margins in resected renal tissue. The device enables discrimination between renal parenchyma and carcinoma by scanning the tissue with an impedance sensor. As illustrated in Fig. 1(b), the electrodes of the impedance sensor were fabricated using a MEMS process. A polyimide (PI) film was attached to a glass wafer to provide mechanical stability during fabrication. Gold (Au) and chromium (Cr) layers with thicknesses of 100 nm and 10 nm, respectively, were sequentially deposited onto the PI film by DC sputtering. Au was selected as the primary electrode material because of its high electrical conductivity and good biocompatibility, whereas Cr was used as an adhesion layer between the Au and PI film. A photoresist (GXR-601) was spin-coated onto the metal-deposited substrate to define the electrode pattern. The electrode pattern was then fabricated through sequential photolithography, development, metal wet etching, and photoresist stripping processes. Figure 1(c) shows the fabricated electrode geometry, which was designed with a line width and spacing of 100 μm. The electrodes consisted of a

detection part and a connection part, which were used for tissue discrimination and electrical connection, respectively. The detection part was designed to measure the electrical characteristics of the parenchyma and carcinoma, whereas the connection part was used to transmit electrical signals to and from the detection part. The total area of the detection part in contact with the tissue was designed to be 7.29 mm^2 (2.7 × 2.7 mm).

The contact force applied to the tissue can induce mechanical deformation, which may distort the measured sensor output (electrical impedance) [17]. Therefore, as shown in Fig. 1(d), a force sensor and wireless monitoring system were integrated into the HDB device to measure the contact force applied to the tissue in real time. The force sensor was positioned adjacent to the impedance sensor, and the measured force data were transmitted to an external monitoring system via Bluetooth communication. The impedance and force sensors were integrated into a single handheld platform to enable simultaneous measurement of tissue electrical impedance and monitoring of the contact conditions during impedance measurements.

Experimental method

Electrical impedance measurements were performed over a wide frequency range from 0.7 kHz to 2 MHz using an impedance analyzer (Gamry Reference 1010E; Gamry Instruments, USA). For data acquisition and control, the impedance analyzer was connected to a laptop via a USB (universal serial bus) interface. The HDB device was electrically connected to the analyzer using a cell cable. During each measurement, a sinusoidal excitation voltage of 200 mVrms was applied across the electrodes of the impedance sensor. The relatively low excitation amplitude was selected in consideration of the potential clinical use of the HDB device to minimize disruption of cell membranes and unintended tissue damage [18].

Preliminary experiment with solutions of various conductivities

In the preliminary experiment, the discrimination capability of the impedance sensor was evaluated using solutions with different conductivities. A standard conductivity solution with a conductivity of 1.28 S/m was used as the initial solution. Solutions with different conductivity values were prepared by serially diluting the initial solution with deionized (DI) water to obtain conductivities of 1.28, 0.64, 0.32, 0.16, 0.08, and 0.04 S/m. As reported in previous studies, the conductivity values selected for this experiment encompass the range reported for various biological tissues [19–21]. For the measurements, the HDB device was fixed to a height controller, and only the electrodes were immersed in the solutions. Measurements were performed sequentially, beginning with the solution with the lowest conductivity and proceeding to the solution with the highest conductivity. After each measurement, the electrodes were thoroughly rinsed with DI water to minimize the influence of residual ions.

Main experiment with human ex-vivo renal tissue

The main experiment was conducted to investigate differences in electrical impedance between renal parenchyma and carcinoma for two major histological subtypes of RCC: clear cell renal cell carcinoma (ccRCC) and papillary renal cell carcinoma (pRCC). As shown in Fig. 2, these two subtypes, which account for the majority of RCC cases, were selected to compare the electrical properties of carcinoma and the corresponding renal parenchyma. Figure 2 illustrates the histology of ccRCC and pRCC. These subtypes exhibit distinct histological characteristics in terms of cytology, tissue architecture, and vascularity. ccRCC is composed of tumor cells with clear, lipid- and glycogen-rich cytoplasm arranged in solid nests, alveoli, and tubules. These structures are characteristically surrounded by an intricate, richly arborizing network of thin-walled capillaries, reflecting the pronounced hypervascularity of ccRCC. In contrast, pRCC is characterized by a papillary or tubulopapillary architecture with fibrovascular cores, which frequently contain aggregates of foamy macrophages, and is considerably less vascular than ccRCC. To minimize changes in the electrical characteristics of the resected renal tissue, electrical impedance measurements were performed on the specimens immediately after resection in the operating room. Electrical impedance was measured at multiple points in both RCC subtypes and their corresponding renal parenchyma. After each measurement, the electrodes were rinsed with deionized (DI) water to remove residual biological material.

Ethics approval and informed consent

This study was approved by the Institutional Review Board (IRB) of Chonnam National University Hospital, Gwangju, Republic of Korea (IRB number: CNUH-2020-072). All methods were carried out in accordance with the relevant guidelines and regulations, and all experimental procedures were performed in accordance with the ethical principles of the Declaration of Helsinki. Renal specimens were obtained from two patients who underwent robot-assisted laparoscopic partial nephrectomy, one with ccRCC and one with pRCC. Written informed consent for participation in this study and for the use of the resected renal tissue was obtained from both patients prior to surgery. To protect participant privacy, all personal identifiers were removed before analysis, and all specimens and data were handled in a de-identified manner.

Results and Discussion

Discrimination capability using solutions with various conductivities

To evaluate the discrimination capability of the impedance sensor integrated into the HDB device, electrical impedance measurements were performed using solutions with different conductivities, as shown in Fig. 3. The magnitude (Z_{mag}), real

part (Z_{real}), and imaginary (Z_{imag}) part of the impedance were clearly distinguishable among solutions with different conductivities over the entire frequency range of 0.7 kHz to 2 MHz. However, the phase exhibited partial overlap among the solutions in certain frequency regions. This behavior may be attributed to the fact that the phase is determined by the relative contributions of Z_{real} and Z_{imag}. The electrical impedance measurements for each solution were repeated 10 times. Among all measurements, the highest standard deviation (SD) was 9.11%, observed for Z_{imag} at a conductivity of 1.28 S/m, whereas all other measurements exhibited lower variations. Overall, the measured parameters (Z_{mag}, Z_{real}, Z_{imag}, and phase) exhibited relatively low SD values across the solutions with different conductivities.

As shown in Fig. 4(a), the measured impedance comprised contributions from both the sample and the electrochemical interface. To separate these contributions, the measured impedance was fitted to an equivalent circuit consisting of the sample resistance (R_s) and capacitance (C_s), as well as the charge-transfer resistance (R_{ct}), double-layer capacitance (C_{dl}), and Warburg impedance (W_{diff}) [22–24]. In this equivalent circuit, R_{ct} represents the charge-transfer kinetics at the electrode–sample interface, C_{dl} represents interfacial charge storage, and W_{diff} represents ionic diffusion and mass transport. The corresponding circuit parameters were extracted by curve fitting to evaluate the electrical response of the sensor to solutions with different conductivities. The R_s values obtained for solutions with conductivities of 1.28, 0.64, 0.32, 0.16, 0.08, and 0.04 S/m were 0.98, 1.86, 3.11, 4.85, 9.64, and 17.13 kΩ, respectively. The corresponding relative SDs were 3.07%, 0.40%, 0.64%, 1.21%, 2.17%, and 0.55%, respectively, indicating high measurement reproducibility.

Z_{mag} and Z_{real} decreased with increasing frequency, whereas Z_{imag} initially decreased and subsequently increased. This behavior can be attributed to the frequency-dependent contributions of the electrochemical interfacial impedance and the bulk impedance of the solution. In the equivalent circuit, R_{ct}, C_{dl}, and W_{diff} represent the components associated with the electrochemical interface at the electrodes, whereas R_s and C_s represent the components associated with the sample. Each parameter was extracted by fitting the measured impedance to the equivalent circuit. As shown in Fig. 4(c)–(h), the calculated Z_{imag} values obtained from the extracted parameters were subsequently compared with the measured data. The contribution of the sample to Z_{imag} increased with increasing frequency, whereas the contribution of the electrochemical interface decreased. Therefore, the initial decrease followed by the subsequent increase in Z_{imag} was attributed to the change in the relative contributions of these components with frequency.

Estimation of the calibration curve

Electrical impedance measurements using the HDB device were performed over a wide frequency range of 0.7 kHz to 2 MHz and required tens of seconds to complete, which limits the applicability of the device for real-time measurements in the operating room (OR). Previous studies have addressed this limitation by using a discrimination index (DI) to identify the

optimal frequency at which the difference in impedance between tissues is greatest **[25].** However, this approach still has limitations because electrical impedance depends on electrode geometry, including electrode size, spacing, and configuration.

Therefore, we developed a method for extracting conductivity from the measured impedance to generalize the sensor output regardless of electrode geometry. Conductivity was estimated using a calibration curve representing the relationship between Z_{mag} and conductivity measured at a specific frequency. The DI was calculated from the electrical impedance of solutions with different conductivities to identify the frequency that provided the greatest distinction among the conductivity levels. The frequency corresponding to the highest DI was selected as the representative frequency. Subsequently, a calibration curve was established based on the relationship between Z_{mag} measured at the selected frequency and the corresponding conductivity. Because Z_{mag} is a representative impedance parameter that incorporates both Z_{real} and Z_{imag}, the conductivity calibration curve was constructed using Z_{mag}. As shown in Fig. 5(a), differences in Z_{mag} were observed among solutions with different conductivities. To determine the frequency that provided the highest discrimination capability among the conductivity solutions, the DI was calculated over the measured frequency range using Eq. (1). In Eq. (1), M and S represent the mean and standard deviation of Z_{mag}, respectively. The subscripts 1.28, 0.64, 0.32, 0.16, 0.08, and 0.04 denote the conductivity values of the standard solutions in S/m. The maximum DI value of 344 was observed at 390 kHz, which was selected as the representative frequency for establishing the relationship between Z_{mag} and conductivity, as shown in Fig. 5(b). As shown in Fig. 5(c), the calibration curve established using the Z_{mag} values measured at 390 kHz and the corresponding solution conductivities exhibited a high coefficient of determination ($R^2 = 0.99$), indicating good agreement between the measured data and the fitted regression line described by Eq. (2). Conductivity was subsequently estimated from the measured Z_{mag} using the linear regression equation obtained from the calibration curve. The accuracy of the calibration curve was further evaluated by comparing the estimated conductivity values with those measured using a commercial conductivity meter. As shown in Fig. 5(d), the conductivity values estimated from the calibration curve exhibited relatively low errors, ranging from 1.19% to 9.29%, compared with the values measured using the conductivity meter.

$$DI = \frac{|M_{1.28}-M_{0.64}|}{S_{1.28}+S_{0.64}} + \frac{|M_{1.28}-M_{0.32}|}{S_{1.28}+S_{0.32}} + \frac{|M_{1.28}-M_{0.16}|}{S_{1.28}+S_{0.16}} + \frac{|M_{1.28}-M_{0.08}|}{S_{1.28}+S_{0.08}} + \frac{|M_{1.28}-M_{0.04}|}{S_{1.28}+S_{0.04}} \quad (1)$$

$$Log\left(Z_{mag} at\ 390\ kHz\right) = -0.8289\left(\left(Log\ (Conductivity)\right)\right) + 3.0916 \quad (2)$$

Electrical impedance of renal tissues in two RCC subtypes

We investigated differences in electrical impedance and conductivity between renal carcinoma and the corresponding renal parenchyma using the impedance sensor for two RCC subtypes: pRCC and ccRCC. Specifically, the electrical impedance and conductivity of pAP (pRCC-adjacent renal parenchyma) and cAP (ccRCC-adjacent renal parenchyma) were compared only with those of pRCC and ccRCC, respectively.

Figure 6 shows the measured Z_{mag} and phase of pRCC, pAP, ccRCC, and cAP under a constant contact force of 0 N. Clear differences in Z_{mag} and phase between renal carcinoma and the corresponding parenchyma were observed for both pRCC and ccRCC. As shown in Fig. 6(a), the electrical impedances of pRCC and pAP were measured over the frequency range of 0.7 kHz to 2 MHz. As the frequency increased, the Z_{mag} values of pRCC and pAP decreased from 45.10 and 92.92 kΩ to 5.21 and 19.82 kΩ, respectively. The SDs of Z_{mag} for pRCC and pAP were relatively large, at 16.79% and 22.24%, respectively. The Z_{mag} of pRCC was lower than that of pAP over the entire measured frequency range, and statistically significant differences between the two tissues were observed at all frequencies ($p < 0.05$). These results indicate that pRCC and pAP can be discriminated based on their electrical impedance over the measured frequency range. As shown in Fig. 6(b), the phase values of pRCC and pAP exhibited different frequency-dependent trends. At low frequencies, the phase of pRCC was higher than that of pAP and decreased with increasing frequency. The phase of pRCC subsequently increased at high frequencies. In contrast, the phase of pAP was lower than that of pRCC at low frequencies but increased substantially with increasing frequency. Consequently, the phase of pAP became higher than that of pRCC at high frequencies.

Figure 6(c) shows the measured Z_{mag} of ccRCC and cAP over the frequency range of 0.7 kHz to 2 MHz. As the frequency increased, the Z_{mag} values of ccRCC and cAP decreased from 2.287 and 3.38 kΩ to 0.87 and 1.21 kΩ, respectively. The SDs of Z_{mag} for ccRCC and cAP were relatively small, at 5.79% and 11.50%, respectively. The Z_{mag} of ccRCC was lower than that of cAP over the entire measured frequency range, and statistically significant differences were observed between the two tissues ($p < 0.05$). The Z_{mag} values of carcinoma and parenchyma were clearly separated over the entire frequency range for pRCC, whereas the two tissues exhibited relatively similar magnitude values for ccRCC. The phase of ccRCC also exhibited a different frequency-dependent trend from that of cAP. At low frequencies, the phase of cAP was higher than that of ccRCC, and the difference between the two tissues gradually decreased with increasing frequency. The phase values of the two tissues became similar over the frequency range of 74.58 to 143.96 kHz. At high frequencies, the phase of ccRCC was higher than that of cAP.

The Z_{mag} of carcinoma was lower than that of the corresponding parenchyma for both pRCC and ccRCC, indicating differences in the conductivity of the carcinoma and parenchyma. As shown in Fig. 4(a), the measured impedance is affected by various electrical characteristics, including R_s, C_s, R_{ct}, C_{dl}, and W_{diff}. Therefore, curve fitting using the equivalent circuit was performed on the measured impedance to compare the estimated sample resistance of each tissue. The extracted R_s values for pRCC, pAP, ccRCC, and cAP were 6.13 ± 0.98, 53.49 ± 14.98, 1.08 ± 0.04, and 1.42 ± 0.12 kΩ, respectively, demonstrating clear differences between the tumor tissues and their corresponding parenchyma.

Comparison of conductivity of renal tissues in two RCC subtypes

Figure 7 shows the estimated conductivities of pRCC, pAP, ccRCC, and cAP. For real-time measurement in clinical applications, the Z_{mag} measured at the optimal frequency of 390 kHz was substituted into the calibration curve described by Eq. (2) in Section 3.2. The estimated conductivities of pRCC, pAP, ccRCC, and cAP were 0.16 ± 0.03, 0.01 ± 0.002, 1.03 ± 0.05, and 0.79 ± 0.09 S/m, respectively. The conductivity of pRCC was higher than that of pAP, and the difference between the two tissues was statistically significant ($p < 0.0001$). Similarly, the conductivity of ccRCC was higher than that of cAP, with a statistically significant difference between the two tissues ($p < 0.0001$). The conductivity of ccRCC was approximately 6.4 times higher than that of pRCC, while the conductivity of cAP was approximately 79 times higher than that of pAP. The conductivity of pRCC was approximately 16 times higher than that of pAP, whereas the conductivity of ccRCC was only approximately 1.3 times higher than that of cAP. Thus, pRCC exhibited substantially higher conductivity than its corresponding parenchyma, whereas the difference in conductivity between ccRCC and cAP was relatively small. These results suggest that the differences in conductivity between ccRCC and pRCC may be associated not only with the intrinsic characteristics of the tumors but also with differences in the microenvironment of each tumor subtype and its surrounding renal parenchyma.

The relatively high conductivity observed in ccRCC may be related to its characteristic vascular structure and tumor microenvironment [26]. ccRCC is closely associated with dysfunction of the von Hippel–Lindau (VHL) protein. When VHL function is impaired, hypoxia-inducible factor (HIF) is stabilized within the cells. Stabilized HIF increases the expression of vascular endothelial growth factor (VEGF), which contributes to the active angiogenesis and high vascular permeability characteristic of ccRCC [27–29]. As shown in the histological images in Fig. 2, ccRCC is characteristically surrounded by a fine and complex capillary network and exhibits prominent hypervascularity. In contrast, pRCC exhibits a relatively sparse vascular distribution. These characteristics may affect the movement of plasma components and water into the extracellular and interstitial spaces. Tissue conductivity can be affected not only by cellular properties but also by the amount of extracellular fluid, tissue water content, ion concentration, and the structure of the extracellular space. In particular, extracellular and interstitial fluids contain electrolytes such as Na^+, K^+, and Cl^- [29,30]. Therefore, an increase in the amount of ion-containing fluid may increase the ionic conduction pathways within the tissue. Thus, VHL dysfunction, HIF stabilization, and increased VEGF expression in ccRCC may alter the extracellular and interstitial fluid environment through increased angiogenesis and vascular permeability [29]. These changes may partly contribute to the high conductivity measured in ccRCC.

The higher conductivity observed in cAP relative to pAP, as well as the difference in conductivity between ccRCC and pRCC, may also be related to differences in the effects of each tumor subtype on the surrounding tissue microenvironment [30,31]. ccRCC generally exhibits higher vascularity and more active angiogenesis than pRCC. Increased vascular permeability associated with the VHL–HIF–VEGF pathway may affect the extracellular and interstitial fluid environment within the tumor. In contrast, pRCC generally exhibits lower vascularity than ccRCC. Therefore, changes in vascular permeability and the associated extracellular and interstitial fluid environment may have a relatively limited effect on the

surrounding parenchyma. This may explain why a large difference in conductivity was observed between pRCC and its corresponding parenchyma, whereas both ccRCC and its corresponding parenchyma exhibited relatively high conductivity, resulting in a smaller difference between the two tissues.

Conclusion

In this study, we developed an HDB device for discriminating renal carcinoma from the corresponding renal parenchyma based on differences in electrical impedance and conductivity. The HDB device integrates an impedance sensor for measuring the electrical properties of tissue and a force sensor for monitoring the contact force applied during impedance measurements. The electrical impedances of pRCC, ccRCC, and their corresponding renal parenchyma obtained from ex-vivo human renal tissues were measured over the frequency range of 0.7 kHz to 2 MHz under the guidance of an expert. The Zmag values of both pRCC and ccRCC were statistically lower than those of the corresponding parenchyma over the measured frequency range ($p < 0.05$). The estimated conductivities of pRCC, pAP, ccRCC, and cAP were 0.16 ± 0.03, 0.01 ± 0.002, 1.03 ± 0.05, and 0.79 ± 0.09 S/m, respectively. These differences may be associated with the distinct histological characteristics and tissue microenvironments of the two RCC subtypes. These results demonstrate that the developed device can discriminate renal carcinoma from the corresponding renal parenchyma based on electrical impedance and conductivity, indicating its potential for intraoperative assessment of surgical margins during partial nephrectomy.

Acknowledgements

We gratefully acknowledge all participants for their contributions to this study

Author contributions

S.L: Conceptualization, Data curation, Formal analysis, Investigation, Methodology, Visualization, Writing – original draft, **Y.P:** Conceptualization, Data curation, Methodology, **S.S.K:** Data curation, Investigation, Resources, **S.B:** Conceptualization, Supervision, **H.S.C**: Conceptualization, Supervision, Methodology, Project administration, Writing – original draft, **J.K:** Conceptualization, Data curation, Formal analysis, Funding acquisition, Investigation, Methodology, Project administration, Supervision, Writing – original draft, Writing – review and editing

Funding

This work was supported by the Korea Medical Device Development Foundation grant funded by the Korea government (the Ministry of Science and ICT, the Ministry of Trade, Industry and Resources, the Ministry of Health & Welfare, the Ministry of Food and Drug Safety) (Project Number: 2410018857, RS-2026-25544764) and by the Korea Institute of Industrial Technology through the project “Development of core technology for smart sensing and digital medical process to support medical surgical field diagnosis” (grant No. KITECH EH-26-0004).

Competing interests

The authors declare no competing interests.

References

[1] Bray, F. et al. Global cancer statistics 2022: GLOBOCAN estimates of incidence and mortality worldwide for 36 cancers in 185 countries. *CA Cancer J. Clin.* **74**, 229–263 (2024).

[2] Capitanio, U. et al. Epidemiology of renal cell carcinoma. *Eur. Urol.* **75**, 74–84 (2019).

[3] Bex, A. et al. European Association of Urology guidelines on renal cell carcinoma: The 2025 update. *Eur. Urol.* **87**, 683–696 (2025).

[4] Shah, P. H. et al. Positive surgical margins increase risk of recurrence after partial nephrectomy for high risk renal tumors. *J. Urol.* **196**, 327–334 (2016).

[5] Mir, M. C. et al. Decline in renal function after partial nephrectomy: Etiology and prevention. *J. Urol.* **193**, 1889–1898 (2015).

[6] Hekman, M. C. H. et al. Intraoperative imaging techniques to support complete tumor resection in partial nephrectomy. *Eur. Urol. Focus* **4**, 960–968 (2018).

[7] Gordetsky, J. et al. Frozen section during partial nephrectomy: Does it predict positive margins? *BJU Int.* **116**, 868–872 (2015).

[8] Holmes, D. et al. Leukocyte analysis and differentiation using high speed microfluidic single cell impedance cytometry. *Lab Chip* **9**, 2881–2889 (2009).

[9] Kim, S. et al. A review of advanced impedance biosensors with microfluidic chips for single-cell analysis. *Biosensors* **11**, 412; https://doi.org/10.3390/bios11110412 (2021).

[10] Hong, J. L., Lan, K. C. & Jang, L. S. Electrical characteristics analysis of various cancer cells using a microfluidic device based on single-cell impedance measurement. *Sens. Actuators B Chem.* **173**, 927–934 (2012).

[11] Yun, J., Kim, J., Cho, H. H. & Lee, J. H. Ex vivo identification of thyroid cancer tissue using electrical impedance spectroscopy on a needle. *Sens. Actuators B Chem.* **261**, 537–544 (2018).

[12] Kim, J. et al. In-vivo detection of the facial nerve from adjacent tissues using microelectrodes with selective passivation during parotidectomy. *IEEE Sens. J.* **22**, 1890–1897 (2022).

[13] Kim, J., Yun, J., Cho, H. H. & Lee, J. H. Enhancement of detection accuracy in depth-profiling using electrochemical impedance spectroscopy-on-a-needle by incremental compensation for immersion depth. *J. Electroanal. Chem.* **838**, 48–56 (2019).

[14] Zhang, H. et al. Electrochemical impedance spectroscopy-based biosensors for label-free detection of pathogens. *Biosensors* **15**, 443; https://doi.org/10.3390/bios15070443 (2025).

[15] Bai, C. et al. Aptamer selection and application in multivalent binding-based electrical impedance detection of inactivated H1N1 virus. *Biosens. Bioelectron.* **110**, 162–167 (2018).

[16] Siuzdak, K. et al. Biomolecular influenza virus detection based on the electrochemical impedance spectroscopy using the nanocrystalline boron-doped diamond electrodes with covalently bound antibodies. *Sens. Actuators B Chem.* **280**, 263–271 (2019).

[17] González-Correa, C. A., Brown, B. H., Smallwood, R. H., Walker, D. C. & Bardhan, K. D. Electrical bioimpedance readings increase with higher pressure applied to the measuring probe. *Physiol. Meas.* **26**, S39–S47 (2005).

[18] Chen, N. C., Chen, C. H., Chen, M. K., Jang, L. S. & Wang, M. H. Single-cell trapping and impedance measurement utilizing dielectrophoresis in a parallel-plate microfluidic device. *Sens. Actuators B Chem.* **190**, 570–577 (2014).

[19] Gabriel, S., Lau, R. W. & Gabriel, C. The dielectric properties of biological tissues: II. Measurements in the frequency range 10 Hz to 20 GHz. *Phys. Med. Biol.* **41**, 2251–2269 (1996).

[20] Laufer, S., Ivorra, A., Reuter, V. E., Rubinsky, B. & Solomon, S. B. Electrical impedance characterization of normal and cancerous human hepatic tissue. *Physiol. Meas.* **31**, 995–1009 (2010).

[21] Prakash, S. et al. Ex vivo electrical impedance measurements on excised hepatic tissue from human patients with metastatic colorectal cancer. *Physiol. Meas.* **36**, 315–328 (2015).

[22] Yun, J., Kim, J., Lee, S., Cho, H. H. & Lee, J. H. Novel method for the detection of the facial nerve using electrical impedance spectroscopy during otologic surgery. *Sens. Actuators B Chem.* **261**, 467–473 (2018).

[23] Linh, N. D., Huyen, N. T. T., Dang, N. H., Piro, B. & Thu, V. T. Electrochemical interface based on polydopamine and gold nanoparticles/reduced graphene oxide for impedimetric detection of lung cancer cells. *RSC Adv.* **13**, 10082–10089 (2023).

[24] Tincu, B. et al. Vertical graphene-based biosensor for tumor cell dielectric signature evaluation. *Micromachines* **13**, 1671; https://doi.org/10.3390/mi13101671 (2022).

[25] Kim, J. et al. Ex-vivo identification of tumor from parenchyma in human liver using electrochemical impedance spectroscopy on a needle. *IEEE Sens. J.* **20**, 14042–14049 (2020).

[26] Raghubar, A. M. et al. Cellular milieu in clear cell renal cell carcinoma. *Front. Oncol.* **12**, 943583; https://doi.org/10.3389/fonc.2022.943583 (2022).

[27] Choueiri, T. K. & Kaelin, W. G. Jr. Targeting the HIF2–VEGF axis in renal cell carcinoma. *Nat. Med.* **26**, 1519–1530 (2020).

[28] Vuong, L., Kotecha, R. R., Voss, M. H. & Hakimi, A. A. Tumor microenvironment dynamics in clear-cell renal cell carcinoma. *Cancer Discov.* **9**, 1349–1357 (2019).

[29] Weis, S. M. & Cheresh, D. A. Pathophysiological consequences of VEGF-induced vascular permeability. *Nature* **437**, 497–504 (2005).

[30] Wagner, M. & Wiig, H. Tumor interstitial fluid formation, characterization, and clinical implications. *Front. Oncol.* **5**, 115; https://doi.org/10.3389/fonc.2015.00115 (2015).

[31] Munson, J. M. & Shieh, A. C. Interstitial fluid flow in cancer: Implications for disease progression and treatment. *Cancer Manag. Res.* **6**, 317–328 (2014).

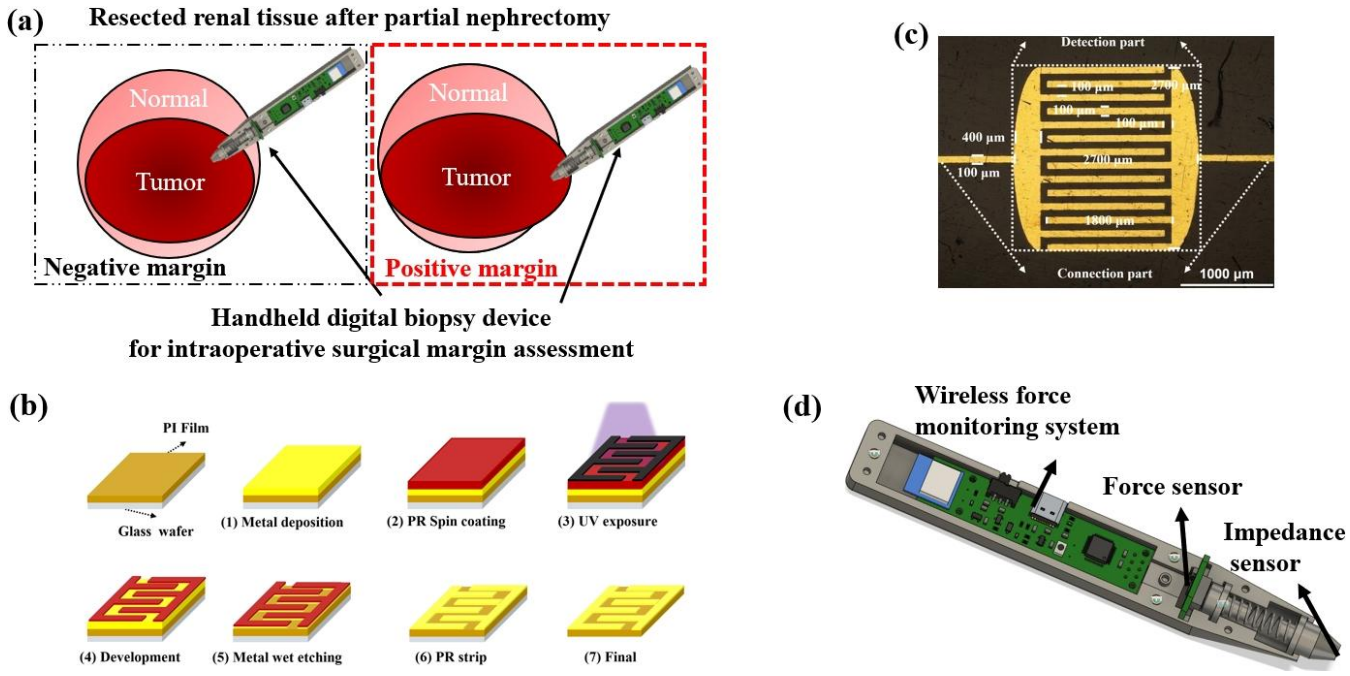


Fig. 1. (a) Conceptual schematic diagram illustrating the assessment of negative and positive surgical margins in resected renal tissue using the handheld digital biopsy device after partial nephrectomy; (b) fabrication procedure for the impedance sensor using a microelectromechanical systems (MEMS) process; (c) optical image of the fabricated impedance sensor showing the detection and connection parts, with a line width and spacing of 100 μm; and (d) configuration of the handheld digital biopsy device integrating the impedance sensor and force sensor.

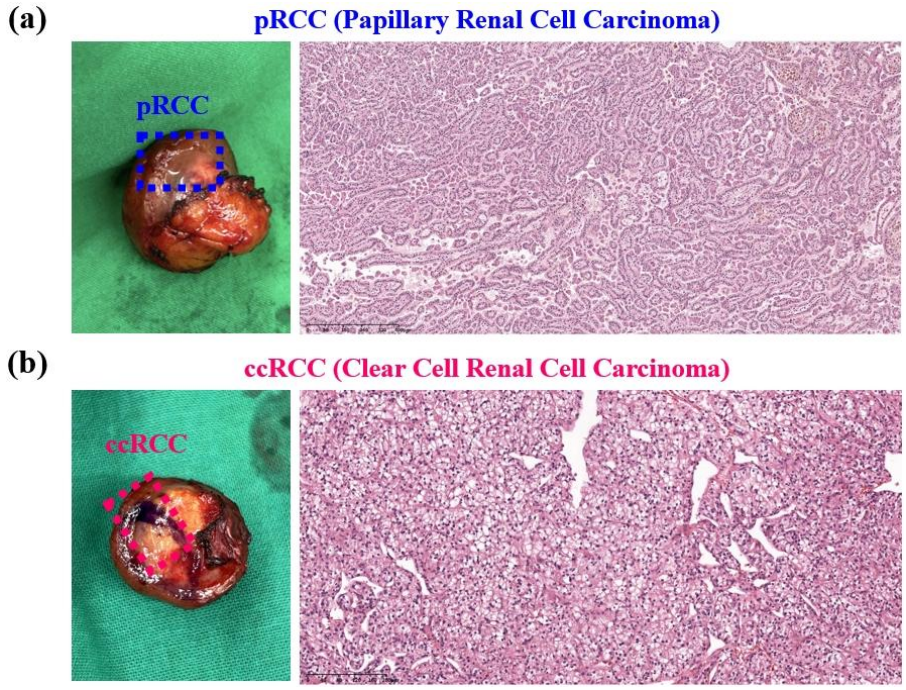


Fig. 2. Histological images of (a) papillary renal cell carcinoma (pRCC) and (b) clear cell renal cell carcinoma (ccRCC) tissues evaluated using the handheld digital biopsy device.

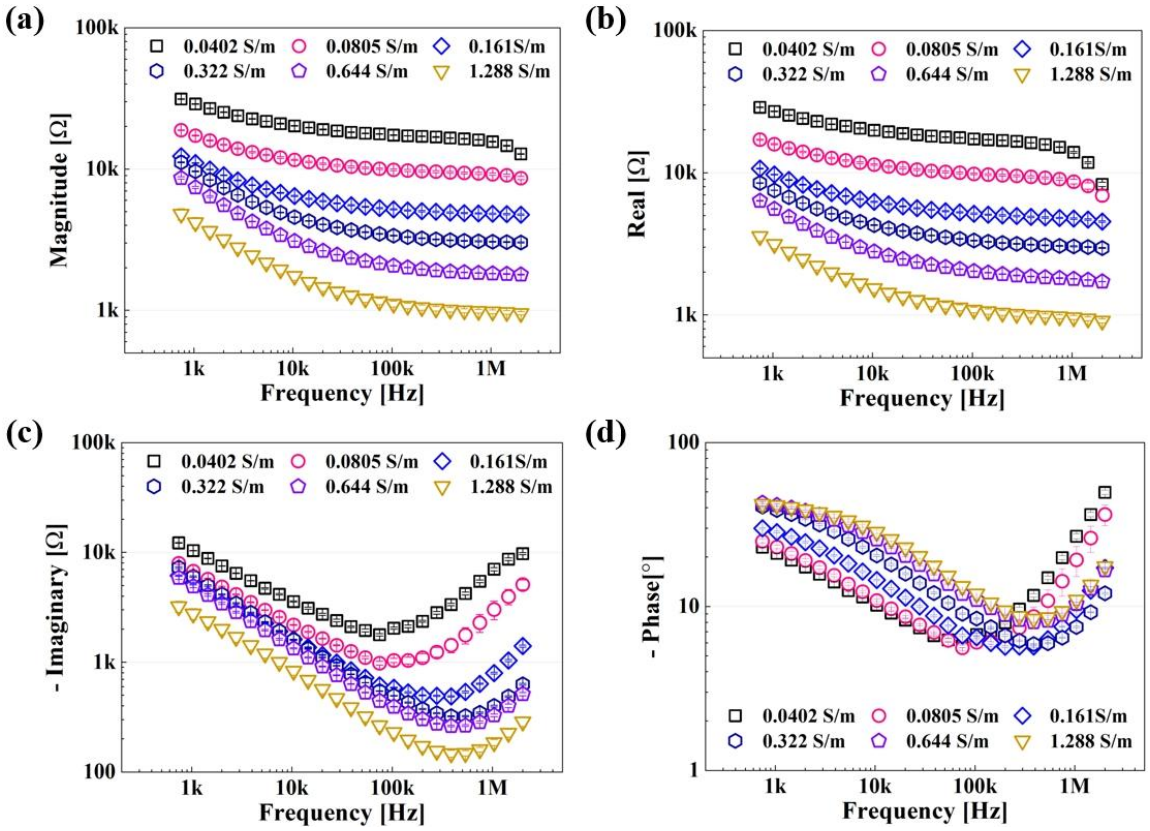


Fig.3 Preliminary evaluation of the discrimination capability of the impedance sensor using solutions with different conductivities over the frequency range of 0.7 kHz to 2 MHz: (a) magnitude, (b) real part of impedance, (c) imaginary part of impedance, and (d) phase.

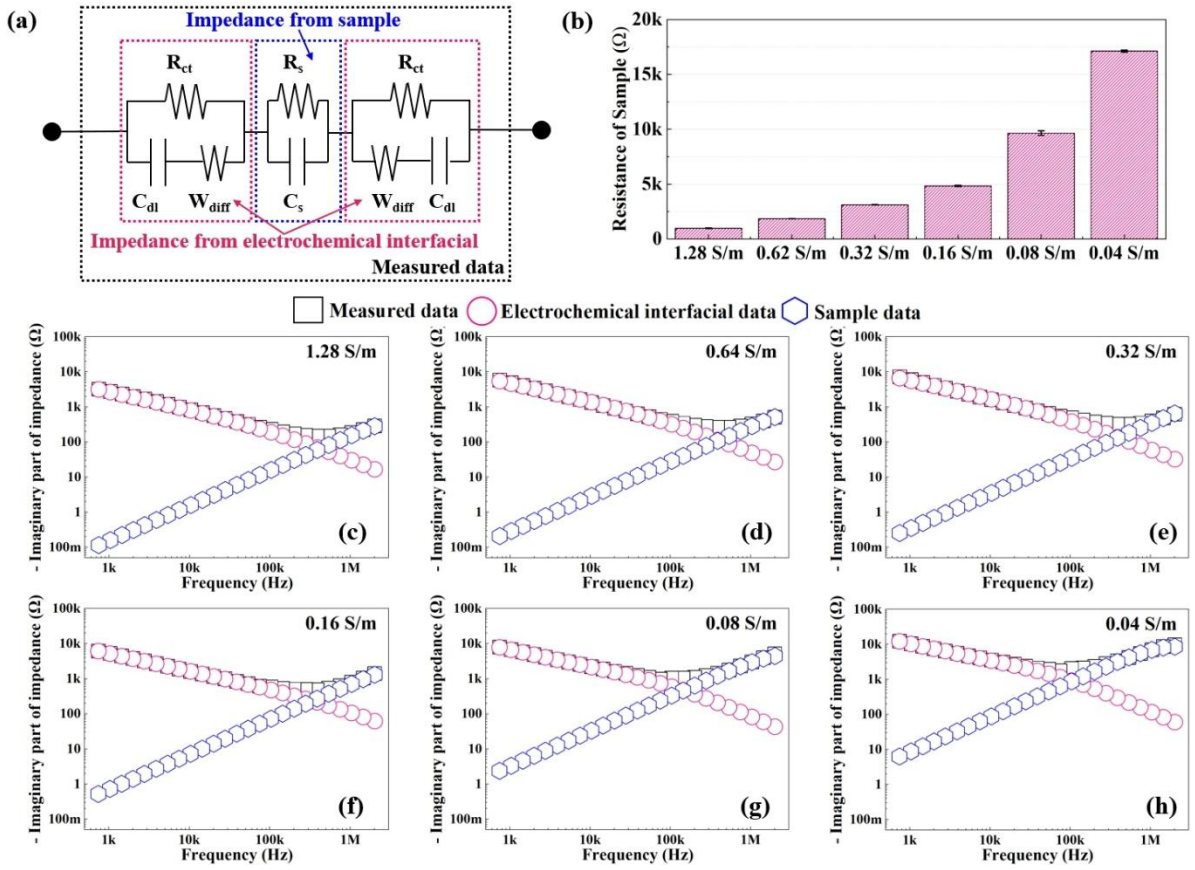


Fig.4 (a) Equivalent circuit representing the electrical characteristics associated with the measured impedance; (b) extracted R_s values for each conductivity solution obtained from the measured impedance through curve fitting to the equivalent circuit; and (c–h) comparison of the measured imaginary part of impedance (Z_{img}) with the calculated Z_{img} components originating from the electrochemical interface and sample at conductivities of 1.28, 0.64, 0.32, 0.16, 0.08, and 0.04 S/m, respectively.

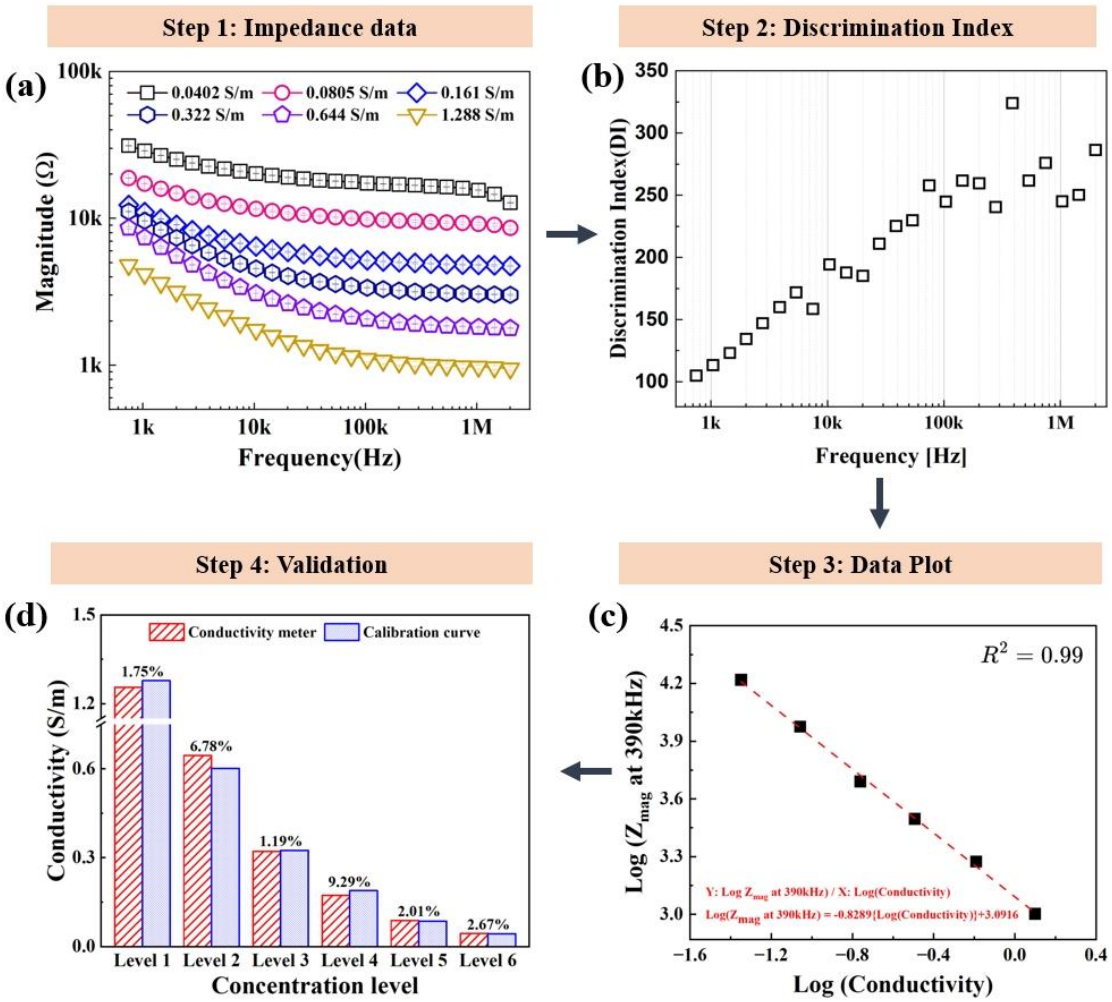


Fig.5 Procedure for estimating conductivity from the measured impedance: (a) measured Z_{mag} for solutions with different conductivities over the frequency range of 0.7 kHz to 2 MHz; (b) calculated discrimination index (DI) for selecting the representative frequency; (c) calibration curve established using Z_{mag} measured at 390 kHz and the corresponding conductivity values; and (d) validation of the estimated conductivity by comparison with measurements obtained using a commercial conductivity meter.

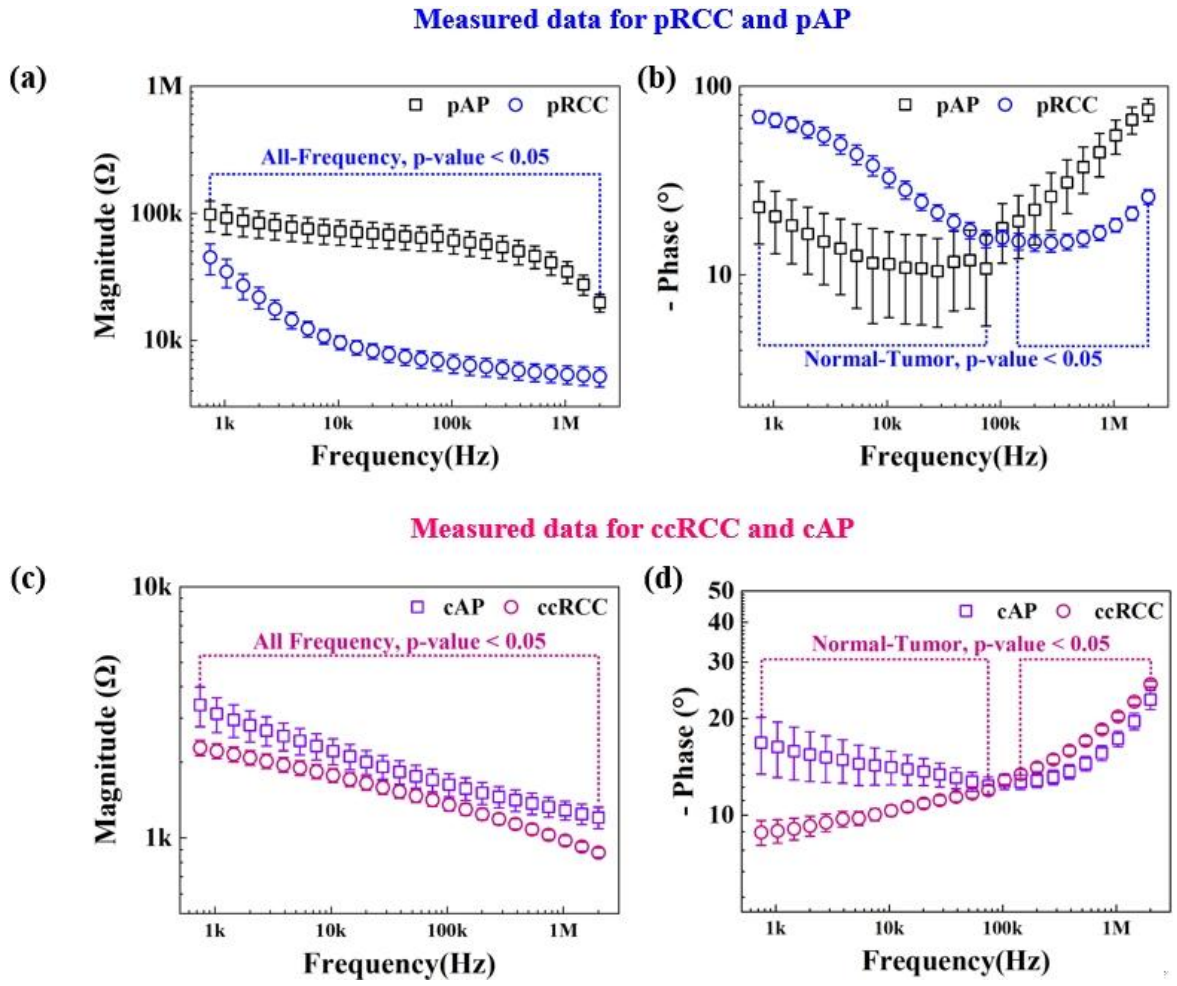


Fig.6 Measured magnitude and phase over the frequency range of 0.7 kHz to 2 MHz for (a and b) papillary renal cell carcinoma (pRCC) and pRCC-adjacent renal parenchyma (pAP) and (c and d) clear cell renal cell carcinoma (ccRCC) and ccRCC-adjacent renal parenchyma (cAP).

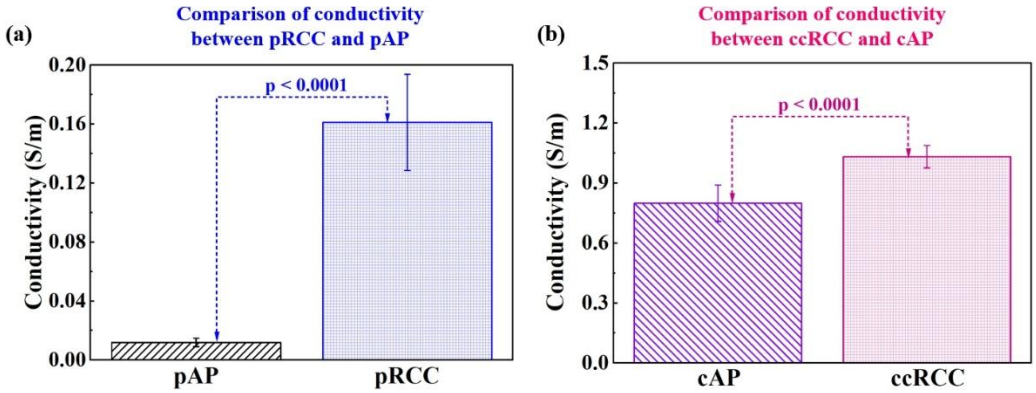


Fig.7 Estimated conductivity of (a) papillary renal cell carcinoma (pRCC) and pRCC-adjacent renal parenchyma (pAP) and (b) clear cell renal cell carcinoma (ccRCC) and ccRCC-adjacent renal parenchyma (cAP).